JOURNAL OF GUIDANCE, CONTROL, AND DYNAMICS
Vol. 33, No. 2, March–April 2010

Endgame Problem Part 2: Multibody Technique and the Tisserand–Poincaré Graph

Stefano Campagnola*
University of Southern California, Los Angeles, California 90089-1191
and
Ryan P. Russell†
Georgia Institute of Technology, Atlanta, Georgia 30332-0150

DOI: 10.2514/1.44290

This two-part series studies the anatomy of the endgame problem, the last part of the spacecraft trajectory before the orbit-insertion maneuver into the science orbit. The endgame provides large savings in the capture Δv, and therefore it is an important element in the design of ESA and NASA missions to the moons of Jupiter and Saturn. The endgame problem has been approached in different ways with different results: the v_∞-leveraging-maneuver approach leads to high-Δv, short-time-of-flight transfers, and the multibody technique leads to low-Δv, long-time-of-flight transfers. This paper series investigates the link between the two approaches, giving a new insight to the complex dynamics of the multibody gravity-assist problem. In this paper we focus on the multibody approach using a new graphical tool, the Tisserand–Poincaré graph. The Tisserand–Poincaré graph shows that ballistic endgames are energetically possible and it explains why they require resonant orbits patched with high-altitude flybys, whereas in the v_∞-leveraging-maneuver approach, flybys alone are not effective without impulsive maneuvers in between them. We then use the Tisserand–Poincaré graph to design quasi-ballistic transfers. Unlike previous methods, the Tisserand–Poincaré graph provides a valuable energy-based target point for the design of the endgame and begin-game and a simple way to patch them. Finally, we present two transfers. The first transfer is between low-altitude orbits at Europa and Ganymede using almost half the Δv of the Hohmann transfer; the second transfer is a 300-day quasi-ballistic transfer between halo orbits of the Jupiter–Ganymede and Jupiter–Europa. With approximately 50 m/s the transfer can be reduced by two months.

Nomenclature

a, e, i	=	semimajor axis, eccentricity, and inclination with respect to the major body
J	=	Jacobi constant
r_a, r_p	=	pericenter and apocenter with respect to the major body
r_π, V_π	=	position and velocity of the spacecraft with respect to the minor body at the closest approach
T	=	Tisserand parameter
X	=	variables in the rotating frame
x	=	variables in the inertial frame
Δv	=	relative velocity of the spacecraft at the minor body
μ	=	gravitational parameter
$\sim$	=	dimensional variables

Subscripts

M	=	minor body
P	=	major body

Introduction

THIS paper is the second of a series of two, in which we study the endgame problem in detail, which is the last part of a trajectory before the insertion maneuver into the science orbit. The work is motivated by the renewed interest by ESA and NASA in missions to the moons of Saturn and Jupiter.

Both the endgame problem and its symmetric problem, the begin-game, are studied and implemented with two different approaches: the v_∞-leveraging maneuver (VILM) and the multibody technique. This paper studies the anatomy of the multibody technique. For more detail we refer to the first paper of the series [1].

In the first section we recall the linked-conics and the patched circular restricted three-body problem (CR3BP) models and show how to transform the linked-conics gravity-assist parameter in a state vector to be used in the CR3BP. We then consider two VILM endgames at Europa that were presented in Part 1 [1] and use them as first guesses for the design of endgames in the CR3BP. The results show that although some VILM solutions cost almost the same, their total Δv might differ by as much as 10% when computed in a more accurate model. In general, the VILM approach should be used for fast preliminary design only if lower-cost longer-transfer solutions are *not* an option. Quasi-ballistic endgames and transfers cannot be designed either using the VILM approach or starting from VILM solutions, hence the need for a more accurate model and design strategy.

In the second section we introduce a Poincaré section in the negative x axis of the rotating reference frame of the CR3BP. Far from the minor body the spacecraft trajectory is very similar to a Keplerian orbit; thus, we can compute the osculating orbital elements of the spacecraft as it crosses the section and plot them in a pericenter-vs-apocenter graph. On the same graph we plot Tisserand parameter level sets: the Tisserand parameter T is an approximation of the Jacobi constant, and it is very accurate when far from the minor body and for small-mass parameters. The result is the Tisserand–Poincaré (T-P) graph, which is a natural extension of the Tisserand graph, as the v_∞ level sets are synonymous to Tisserand level sets, noting that $T = 3 - v_\infty^2$ (see Appendix B). Yet the Tisserand level sets extend beyond the v_∞ curves well into the regions where v_∞ is not feasible in the linked-conics model ($v_\infty^2 < 0$ if $T > 3$). Therefore, when considering the conservation of the Tisserand parameter, the T-P

Presented at the AIAA/AAS 2009 Space Flight Mechanics Meeting, Savannah, GA, 8 February 2009–12 February 2020; received 20 April 2009; revision received 2 November 2009; accepted for publication 2 November 2009.

*Ph.D. Student, Aerospace and Mechanical Engineering, 854 Downay Way; stefano.campagnola@missionanalysis.org. Member AIAA.

†Assistant Professor, Guggenheim School of Aerospace Engineering, 270 Ferst Drive; ryan.russell@gatech.edu. Member AIAA.

graph demonstrates that ballistic transfers between moons are energetically possible despite the contrary conclusion derived from linked-conics theory. This is the first important result of the T-P graph.

In the third section we analyze the T-P graph in more detail. We use it to explain the multimoon orbiter [2] and to explain the anatomy of multibody techniques in general. We focus on ballistic endgames and question the need for multiple flybys and resonant orbits, noting that ballistic transfers do not change the Jacobi constant and hence do not change the arrival speed at the minor body (the *ballistic endgame paradox*). Then we use the T-P graph to solve the paradox, showing that at low energy levels, high-altitude flybys of the minor body are the only ballistic mechanism to move along the Tisserand curves and to reach the target altitude at the minor body.

In the last section we design transfers between Europa and Ganymede. Using the considerations from the previous section, we find trajectories that move through the graph in the shortest time and reach a prespecified target point on the T-P graph, which is the intersection of the Tisserand level sets of the endgame at Europa and begin-game at Ganymede. In particular, we compute a transfer from a circular orbit at Ganymede to a circular orbit at Europa for comparison with the VILMs solutions. We also compute a transfer between a halo orbit at Ganymede and a halo orbit at Callisto; in both cases the T-P graph provides an estimate of ΔV. We argue that although the total cost might increase in the full-ephemeris model due to the fourth-body perturbations, noncircular orbits, and change-of-plane maneuvers, a robust optimization algorithm should reduce the conservatively estimated costs with the introduction of several small midcourse maneuvers. Finally, we recall that in the Jupiter system long-time-of-flight trajectories are prohibited by the radiation exposure.

Endgames from Linked 2BP to CR3BP

The conventional method for designing endgame trajectories is by patching v_∞-leveraging maneuvers (VILMs) in the linked-conics model [1,3,4]. Yet near-ballistic endgames have been designed only in more accurate models, such as the restricted five-body problem [2] or the full-ephemeris model [5]. In this work, we use the circular restricted three-body problem (CR3BP) model to design ballistic endgames, and we use patched CR3BP models to design transfers between moons.

In this section we briefly recall the linked-conics and the (patched) CR3BP models, and we show how to reproduce a linked-conics gravity assist in the planar CR3BP. We then consider two very similar Europa endgames in the linked-conics model (designed using the leveraging graphs [1]) and optimize them in the CR3BP model. The results give insight into the difference between the two models and into the limitations of the lower-fidelity VILM approach when designing long-flight-time, low-cost endgame trajectories.

Linked-Conics and CR3BP Models

The *linked-conics model* (or zero-radius sphere of influence, patched-conics model) is often used in the design of multiple-gravity-assist trajectories. The spacecraft and the minor bodies move as point masses on Keplerian orbits around the major body. If the spacecraft reaches one of the minor bodies, a gravity assist takes place and is modeled as an instantaneous change in the direction of the relative velocity v_∞ by an angle

$$\delta = 2\arcsin\frac{\tilde{\mu}_M}{\tilde{\mu}_M + \tilde{r}_\pi \tilde{v}_\infty^2} \tag{1}$$

Here and in the rest of the paper, the tilde indicates dimensional quantities; variables without the tilde have been normalized using the usual space, time, and mass scale factors:

$$l^* = \tilde{a}_M, \qquad t^* = \sqrt{\frac{\tilde{a}_M^3}{\tilde{\mu}_P + \tilde{\mu}_M}} \qquad m^* = \tilde{m}_M + \tilde{m}_P$$

Lowercase letters refer to variables in the inertial reference frame, and uppercase letters refer to variables in the rotating reference frame.

In the CR3BP model the gravity of both the major body and the minor body affects the motion of the spacecraft at all times. The major and minor bodies move in circular motion around their barycenter, and the spacecraft is massless. The equations of motion for the spacecraft are usually expressed in the rotating nondimensional reference frame [6]:

$$\begin{cases} \ddot{X} - 2\dot{Y} = \frac{\partial \Omega}{\partial X} \\ \ddot{Y} + 2\dot{X} = \frac{\partial \Omega}{\partial Y} \\ \ddot{Z} \qquad\quad = \frac{\partial \Omega}{\partial Z} \end{cases} \tag{2}$$

$$\Omega(X, Y, Z) \equiv \frac{1}{2}(X^2 + Y^2) + \frac{1-\mu}{R_1} + \frac{\mu}{R_2} + \frac{1}{2}(1-\mu)\mu \tag{3}$$

where

$$R_1 = \sqrt{(X+\mu)^2 + Y^2 + Z^2}$$

and

$$R_2 = \sqrt{(X+\mu-1)^2 + Y^2 + Z^2}$$

are the distances to the primaries, and

$$\mu = \mu_M = \frac{\tilde{m}_M}{\tilde{m}_M + \tilde{m}_P}$$

is the mass parameter. It is well known [6,7] that the system of Eqs. (2) has one integral of motion, the Jacobi constant:

$$J = 2\Omega - V^2 = (X^2 + Y^2) + 2\frac{1-\mu}{R_1} + 2\frac{\mu}{R_2} + (1-\mu)\mu - V^2 \tag{4}$$

where $V^2 = (\dot{X}^2 + \dot{Y}^2 + \dot{Z}^2)$ is the velocity in the rotating frame. The Jacobi constant is used to define regions of motion. The system of Eq. (2) also has five fixed points: the Lagrangian points L_i ($i = 1, \ldots, 5$). In the rest of the paper, unless specified, we use the *planar* CR3BP, noting that the spacecraft trajectory is very close to the minor-body orbital plane for the applications of interest here (i.e., missions to the Jupiter's or Saturn's moons).

In the design of transfers between moons, several minor bodies affect the spacecraft trajectory. In this case we use the *patched-CR3BP model*, i.e., we split the trajectory in phases where only one minor body at a time affects the motion of the spacecraft around the major body. In each phase we use the corresponding minor body in the CR3BP model, and the boundary points of contiguous phases are patched together, sometimes using impulsive maneuvers.

Flyby Models

In this section we reproduce a linked-conics gravity assist in the CR3BP. In particular, we use the parameters of the linked-conics gravity assist to generate the vector state of the spacecraft at r_π, the closest approach to the minor body. We focus on the planar case, because we will use the results to reproduce VILMs in the CR3BP. Figure 1 shows the schematic of the direct and retrograde gravity assists.

From the velocity $v_{(i)}$ and flight-path angle γ of the spacecraft just before the encounter, we find

$$v_\infty = \sqrt{1 + v_{(i)}^2 - 2v_{(i)}\cos\gamma}, \qquad \beta_{(i)} = \arcsin\frac{v_{(i)}\cos\gamma}{v_\infty} \tag{5}$$

The gravity-assist parameters r_π and σ ($\sigma = 1$ for direct gravity assists and $\sigma = -1$ for retrograde gravity assists) provide the deviation angle with Eq. (1) and the norm and direction of the velocity at pericenter v_π, as shown in Fig. 1 and in the following equations:

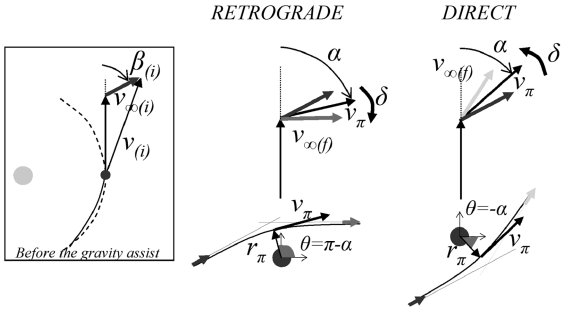

Fig. 1 Direct and retrograde gravity assists.

$$v_\pi = \sqrt{v_\infty^2 + 2\mu/r_\pi}, \qquad \alpha = \beta_{(i)} - \sigma\delta/2 \tag{6}$$

Now we can write the state $s = (x, y, \dot{x}, \dot{y})$ of the spacecraft at the closest approach in the inertial reference frame centered in the minor body. Always referring to Fig. 1, we find

$$\theta = -\alpha + (1-\sigma)\pi/2$$
$$s = (r_\pi \cos\theta, r_\pi \sin\theta, -\sigma v_\pi \sin\theta, \sigma v_\pi \cos\theta) \tag{7}$$

Finally, we apply the transformation of coordinate (see Appendix A) to find the state vector in the rotating reference frame:

$$S = ((1-\mu) + r_\pi \cos\theta, r_\pi \sin\theta,$$
$$-(\sigma v_\pi - r_\pi)\sin\theta, (\sigma v_\pi - r_\pi)\cos\theta) \tag{8}$$

We now consider the special case $\beta_{(i)} = 0$ (the case when the v_∞ vector is aligned with the body velocity vector), which we use in the next section. From Eqs. (6) and (7) we find

$$\theta = -\frac{\pi}{2} + \sigma\left(\frac{\pi}{2} + \frac{\delta}{2}\right) \tag{9}$$

Endgame Optimization in the CR3BP

In this section we compute two endgames in the CR3BP. We take two VILM endgames at Europa presented in Campagnola and Russell [1], reproduce them in the CR3BP, and use them as first guesses for an optimization algorithm that minimizes the total Δv.

The first endgame is a sequence of long-transfer VILMs: $3{:}2_1^+$, $4{:}3_0^+$, and $5{:}6_0^+$, where the plus sign refers to a long-transfer VILM. The second endgame is a sequence of short-transfer VILMs: $3{:}2_1^-$, $4{:}3_0^-$, $5{:}6_0^-$, where the minus sign refers to a short-transfer VILM. Both endgames require approximately 150 m/s to decrease the v_∞ from 1.8 km/s to approximately 0.8 km/s, and both endgames are composed of VILMs in which $\beta_{(i)} = 0$. However, the long-transfer VILMs are linked by direct gravity assists ($\sigma = 1$), and the short-transfer VILMs are linked by retrograde gravity assists ($\sigma = -1$).

As a consequence, Eq. (9) shows that the closest approaches of the first endgame occur on the L2 side ($-\pi/2 < \theta < \pi/2$), and the closest approaches of the second endgame occur on the L1 side ($\pi/2 < \theta < 3\pi/2$). Although the two endgames have similar costs, sequence of resonances, and transfer time, they are significantly different in the region around the minor body, and they belong to two different basins of attraction for the optimization problem in the CR3BP. This subtlety justifies the choice of optimizing both of them.

The trajectory optimization problem in the CR3BP is formulated as a nonlinear parameter optimization problem in which the dynamics constraints (equations of motion) are solved implicitly. The control variables are the times, altitudes $r_\pi - \tilde{r}_M$, speeds v_π, and angles θ of all the closest approaches and the times of the midcourse maneuvers.

The optimizer first propagates the states of every close approach backward and forward in time until the midcourse-maneuver time. The position of the last point of the forward propagation is then constrained to match the position of the last point of the backward propagation from the next-closest approach.[‡] The corresponding velocities are free, but their difference in norm is added to the merit function.

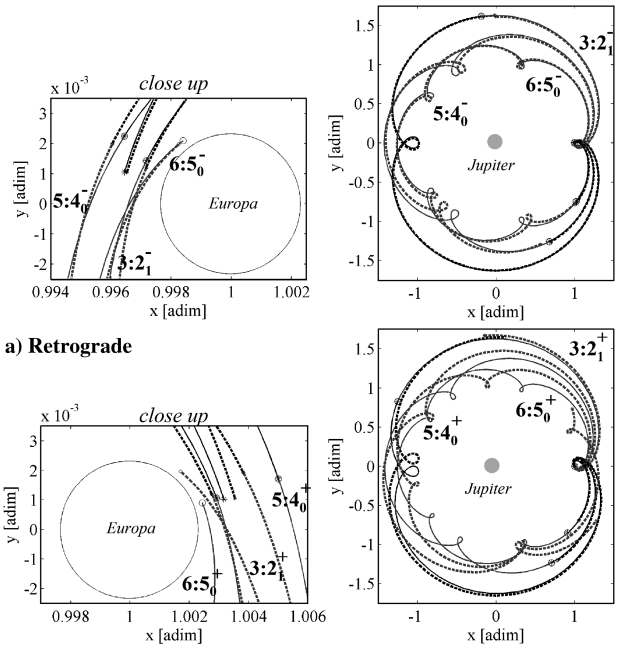

Fig. 2 Long-transfer (direct) and short-transfer (retrograde) endgames at Europa optimized in the CR3BP (solid lines). Initially the VILM solutions are used to find the times of the midcourse and the states and times of the spacecraft at the close approaches. Those states are then propagated backward and forward in time in the CR3BP generating the first-guess solutions (dash lines) for the optimization problem.

As we are ultimately interested in comparing the VILM solutions with the CR3BP endgame, we add constraints to fix the boundary conditions. In particular, we constrain the first closest approach to keep the first guess $\beta_{(i)}$ and v_∞, and we constrain the last closest approach to a given altitude and v_∞.

The first guess is generated using the VILM approach. The VILM solutions provide the times of the midcourse maneuvers and the flyby times, altitudes, and v_∞. Equations (6), (8), and (9) are used to compute the angles θ and the velocities v_π. Finally, the parameter optimization problem is fed into the MATLAB solver `fmincon`, which implements a sequential quadratic programming method. For both endgames, Fig. 2 shows the initial guesses (dashed lines) and the optimized solutions (solid lines). The total cost of the optimized long-transfer endgame is 147 m/s (the VILM solution costs 154 m/s) with a time of flight of 47.0 days, and the cost of the optimized short-transfer endgame is 165 m/s (the VILM solution costs 155 m/s) with a time of flight of 45.4 days.

Limitations of the VILM Approach

The VILM approach is very fast and intuitive, and we envision using it for preliminary design of endgame and begin-game trajectories whenever long-transfer-time low-cost solutions are not an option. However, the previous section showed that the VILM approach has some important limitations that deserve attention.

First, the cost of the VILM endgames can be off by up to ±5% when compared with the more accurate CR3BP solutions. (These values are consistent with the ±10% difference observed during the design of the Cassini tour when comparing Δv costs in the linked-conics model with more accurate models.[§]) We expect this

[‡]Because the problem is formulated in the rotating reference frame, the approach is robust despite the several revolutions (in the inertial frame) that occur between the flybys and the midcourse maneuvers.

[§]Private communication with N. Strange, 2008.

error to increase as more resonances and high-altitude gravity assists are added.

Second, whereas the VILM approach estimates approximately the same Δv for the short-transfer solution and the long-transfer solution, the CR3BP shows that one kind of transfer is preferable (the long transfer in the case shown in the previous section).

Finally, and most important, quasi-ballistic endgames cannot be found by simply designing a VILM endgame and optimizing it in the CR3BP. The linked-conics approach cannot explain the existence of ballistic endgames (not even in the limit of infinite transfer time in which a minimum $\Delta v \neq 0$ can be computed [1]). In addition, the last section showed that the VILM solutions do not converge to quasi-ballistic endgames in the CR3BP. In fact, the multiresonant transfers are chaotic in nature when the design space is plagued by multiple local minima [8] that can easily trap gradient-based optimizers. Clearly, local minima exist in the CR3BP when using the VILM as an initial guess, but it is unrealistic for the optimizer to climb out of that basin en route to quasi-ballistic solutions. Instead, we should seek solutions that start in the correct basin.

For the above reasons, we seek to further our understanding of the dynamics of near-ballistic endgame transfers. Ultimately, we seek systematic methods and tools to design such transfers. Whereas the patched CR3BP is the first step toward solutions in a fully perturbed n-body model, the CR3BP indeed captures the dominant dynamics. Further, the system is Hamiltonian, allows for rapid computations, and preserves the Jacobi constant (or, equivalently, in the case of this study, the Tisserand parameter).

Tisserand Parameter and the T-P Graph

In this section we introduce the T-P graph (named after Tisserand and Poincaré). The graph is a fundamental tool that provides dynamical justification for the multibody technique and can be used to design quasi-ballistic transfers between moons. The T-P graph is built plotting Poincaré sections of different CR3BP models in one unique r_a–r_p graph. The level sets of the respective Tisserand parameters are also plotted in the same graph. The result is the T-P graph, which can be interpreted as an extension of the Tisserand graph [9,10] from the linked-conics model to the patched-CR3BP model.

Poincaré Section

The first step in building the T-P graph is the introduction of a Poincaré section in the negative x axis of the rotating reference frame of each CR3BP. When the spacecraft crosses the Poincaré section, far from the minor body, its trajectory is very well approximated by a Keplerian orbit around the major body. From the state vector at the crossing point, we compute the osculating pericenter and apocenter relative to the main body, which we plot in a r_a–r_p graph, similar to the one described in Campagnola and Russell [1]. Figure 3 shows a schematic of the Poincaré section and the corresponding r_a–r_p graph.

Tisserand Parameter

On the same plot (Fig. 3), we want to plot the level sets of constant Tisserand parameter. The Tisserand parameter T is a function of the semimajor axis a (in normalized units, $a = \tilde{a}/\tilde{a}_M$), inclination i, and eccentricity e of a spacecraft orbiting a major body [11]:

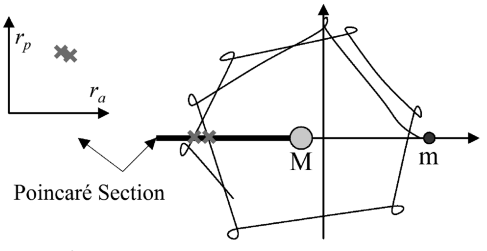

Fig. 3 Poincaré section for the definition of the T-P graph (schematic).

$$T(a, e, i) = \frac{1}{a} + 2\sqrt{a(1-e^2)}\cos i \tag{10}$$

In this work we consider the planar problem and rewrite Eq. (10) as a function of the pericenter and apocenter only:

$$T(r_a, r_p) = \frac{2}{r_a + r_p} + 2\sqrt{\frac{2r_a r_p}{r_a + r_p}} \tag{11}$$

The Tisserand parameter remains approximately constant even after a close encounter with a minor body. This is known as the *Tisserand criterion* [11]. It is well known, in fact, that the Tisserand parameter is an approximation of the Jacobi constant J of the CR3BP: i.e., $T \approx J$.

The approximation is increasingly accurate for smaller mass parameters μ and when the spacecraft is far from the minor body (e.g., when it crosses the Poincaré section defined previously). In Appendix B we show how to derive the Tisserand parameter from the Jacobi constant; similar derivations are found in the literature [11,12].

T-P Graph

Now we are ready to plot the level sets of the Tisserand parameter onto the r_a–r_p graph. We start plotting the four level sets $T = J_{Li}$ ($i = 1, \ldots, 4$), where J_{Li} is the value of the Jacobi constant associated with the ith Lagrangian points (note that $J_{L4} = J_{L5} = 3$). The level sets divide the r_a–r_p graph into regions of motion, as shown in Fig. 4.

As the spacecraft crosses the Poincaré section, the osculating orbital elements are represented with a point on the T-P graph. If the point is in the region I^i, the spacecraft position is bounded in a region close to the major body and no transfer to the minor body is possible. Similarly, if the spacecraft is in the region I^e, the spacecraft is bounded in a region far from the major body and no transfer to the minor body is possible.

Transfers to the minor body are possible only when the spacecraft is in the regions II^i, II^e, or III. In particular, we expect low-energy transfer and capture trajectories to occur in the region II^i (if coming from the inner moons) or II^e (if coming from the outer moons).

Note that inside the box $r_p < 1$ and $r_a > 1$ (within region III) we can also plot the constant v_∞ level sets, as done in the Tisserand graph [10]. The v_∞ level sets overlap with the constant Tisserand level sets. Then we can think of the Tisserand level sets as a J level set or $C3 = v_\infty^2$ level sets. In fact, it can be proved that (see Appendix B)

$$T = 3 - v_\infty^2 \approx J$$

In the r_a–r_p graph we can plot curves at constant resonance n:m (where n is the number of body revolutions and m is the number of spacecraft revolutions), which are lines with slope -1 [1]:

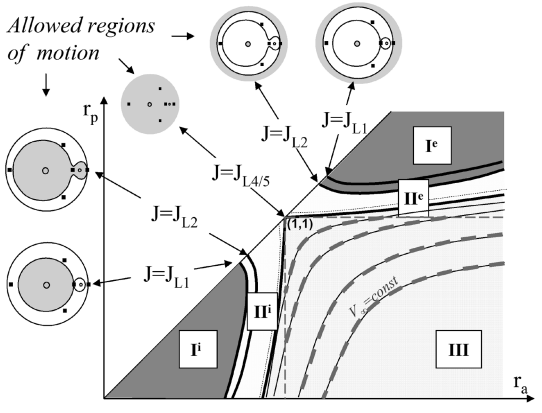

Fig. 4 Tisserand parameter level sets on the T-P graph and corresponding regions of motion in the CR3BP (schematic).

$$a = \left(\frac{n}{m}\right)^{2/3} \rightarrow r_p = -r_a + 2\left(\frac{n}{m}\right)^{2/3}$$

To study transfers between minor bodies, we plot several Tisserand level sets on the same graph, each in the dimensioned coordinates of the corresponding minor body. The Tisserand parameter with respect to the minor body M is

$$T_M = \frac{2\tilde{a}_M}{\tilde{r}_a + \tilde{r}_p} + 2\sqrt{\frac{2\tilde{r}_a\tilde{r}_p}{(\tilde{r}_a + \tilde{r}_p)\tilde{a}_M}} \tag{12}$$

Finally, we include a grid that shows the Δv required to change the pericenter/apocenter using an impulsive maneuver.

The result is the T-P graph, which we show in Fig. 5b. In Fig. 5a we plot the r_a–r_p Tisserand graph [1]. We see how the extension from a linked-conics model (for the Tisserand graph) to patched-CR3BP model (T-P graph) results in level sets that extend over the feasible domain of the Tisserand graph. As a consequence, even low-energy (low-v_∞) level sets reach very high apocenters.

Figure 6 shows the T-P graph for the Saturn system. We can see that the low-energy level sets (regions II^e and II^i) of any two moons cross, in contrast to the linked-conics model, in which ballistic intermoon transfers are only possible for v_∞ greater than that of the corresponding Hohmann transfer. From an *energetic* point of view, a ballistic transfer between any two moons in the patched CR3BP is always possible. This does not guarantee that such transfers can be found, especially within a practical transfer time. Some recent works demonstrate that such transfers can exist [13].

The intersection point between the Tisserand level sets of two different moons is the solution of the system

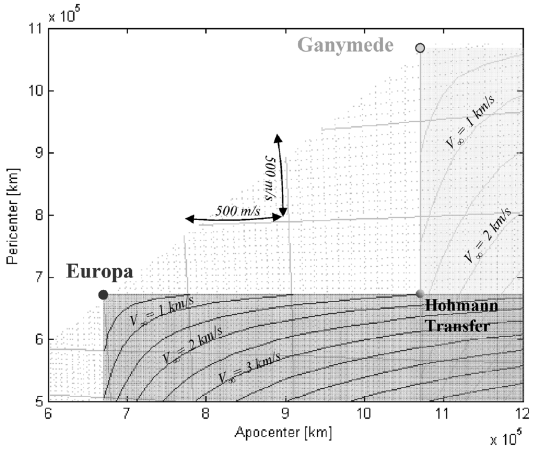

a) Tisserand Graph

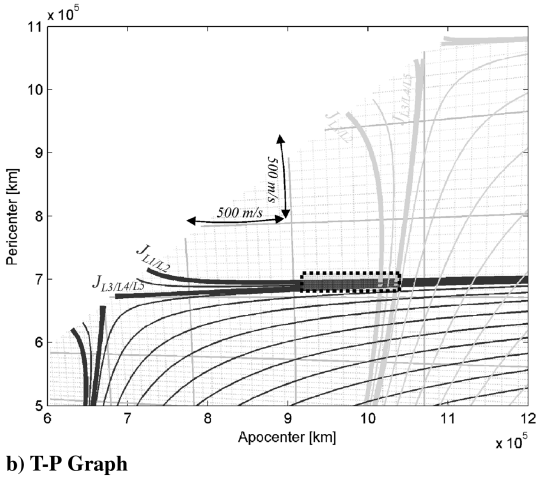

b) T-P Graph

Fig. 5 Graphs: a) Tisserand and b) Tisserand–Poincaré.

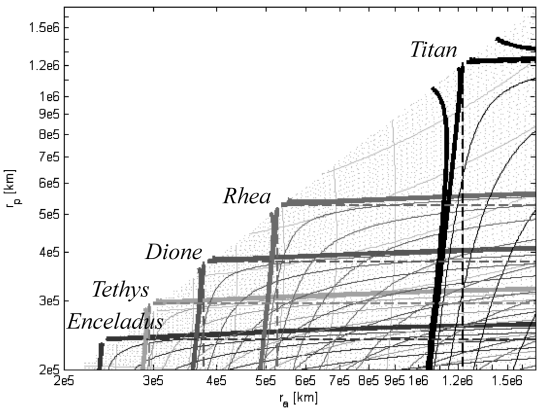

Fig. 6 T-P graph of the Saturn system.

$$\begin{cases} T_{M1} = \frac{2\tilde{a}_{M1}}{\tilde{r}_a+\tilde{r}_p} + 2\sqrt{\frac{2\tilde{r}_a\tilde{r}_p}{(\tilde{r}_a+\tilde{r}_p)\tilde{a}_{M1}}} \\ T_{M2} = \frac{2\tilde{a}_{M2}}{\tilde{r}_a+\tilde{r}_p} + 2\sqrt{\frac{2\tilde{r}_a\tilde{r}_p}{(\tilde{r}_a+\tilde{r}_p)\tilde{a}_{M2}}} \end{cases} \tag{13}$$

where we solve for r_a and r_p, giving the desired T_{M1} and T_{M2} along with the $\tilde{a}_{M1}$ and $\tilde{a}_{M2}$ for the systems of interest. We emphasize that the T-P graph provides a reliable energy-based strategy to patch the two CRTBP systems. The patch-point target provides a significant advantage over prior multibody design methodologies.

Three-Dimensional T-P Graph

In this section we consider the 3-D case, in which the Tisserand parameter is function of the apocenter, the pericenter, and the inclination:

$$T_M = \frac{2\tilde{a}_M}{\tilde{r}_a + \tilde{r}_p} + 2\sqrt{\frac{2\tilde{r}_a\tilde{r}_p}{(\tilde{r}_a + \tilde{r}_p)\tilde{a}_M}}\cos i \tag{14}$$

The 3-D T-P graph can be used to visualize families of asteroids in the solar system [14] or to analyze missions such as the Solar Orbiter that use resonant gravity assists at Venus to reach high inclinations

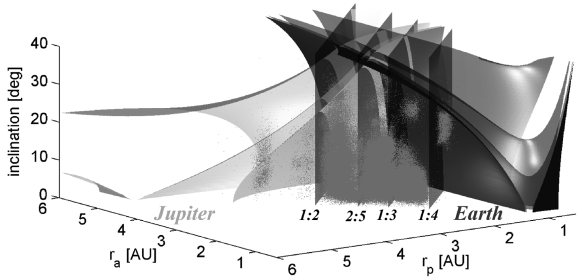

Fig. 7 Example of a 3-D T-P graph: the Earth and Jupiter level sets and the main-belt asteroids.

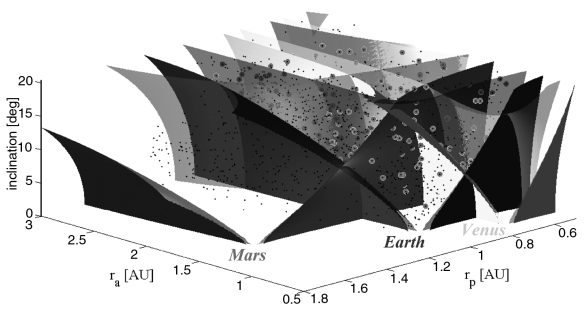

Fig. 8 Examples of a 3-D T-P graph: the near-Earth asteroids and, among those, the potentially hazardous asteroids.

over the ecliptic [15]. Figure 7 shows the Earth and Jupiter Tisserand level sets and the main-belt asteroids. Most of the main-belt asteroids are outside the surfaces $T_{\text{Earth}} = J_{L1\text{Earth}}$ and $T_{\text{Jupiter}} = J_{L1\text{Jupiter}}$. We also can see the Kirkwood gaps at the resonances [16] 1:4, 3:1, 2:5, and 1:2. Figure 8 shows the near-Earth asteroids and, among those, the potentially hazardous asteroids. We can see that the potentially hazardous asteroids are all within the level set $T_{\text{Earth}} = J_{L1\text{Earth}}$.

Anatomy of the Multibody Technique

In this section we use the T-P graph to explain how the multibody techniques are used to design endgame trajectories. The multibody techniques propagate the state of the spacecraft in multibody dynamics, targeting high-altitude encounters with a minor body to achieve the most suitable effect (typically a reduction or an increase of the one of the apses). Trajectories designed with multibody techniques include the SMART-1 mission to the moon [5] and the multimoon orbiter by Ross and Lo [2].

Multimoon Orbiter

The multimoon orbiter is a trajectory designed by Ross and Lo [2] for a mission to the Jovian moons. The trajectory was computed in the planar restricted five-body problem.

Figure 9a shows the Tisserand graph of the trajectory in the Jupiter system. The orbital elements vary mostly during short time intervals when the spacecraft approaches a moon, making the Tisserand graph difficult to read. The osculating pericenter and apocenter are often outside the boundaries ($\tilde{r}_a > \tilde{r}_M$ and $\tilde{r}_p < \tilde{r}_M$) imposed by the linked-conics model.

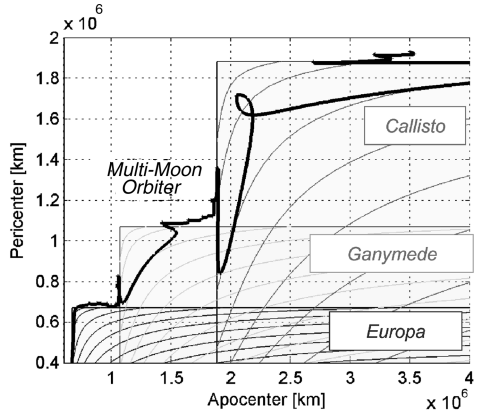

a)

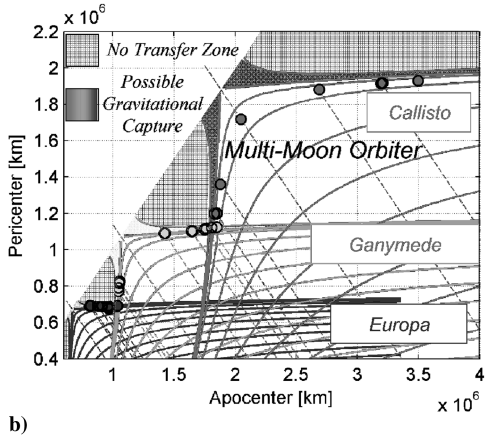

b)

Fig. 9 Multimoon orbiter [2] trajectory osculating parameters plotted in the a) r_a–r_p conventional Tisserand graph and b) T-P graph. The T-P graphs shows that the trajectory jumps between resonances and are mostly ballistic. We can see the no-transfer zones (light gray) and the capture zones. At the end of the trajectory, the spacecraft is inside the Europa capture zone.

We now represent the same trajectory with the T-P graph. We first split the trajectory in three parts, depending on the dominating perturbing body. The first part is dominated by Callisto, the second by Ganymede, and the third by Europa. For each part we place a Poincaré section on the negative x axis of the corresponding rotating reference frame and build the T-P graph of the transfer. The result is shown in Fig. 9b. We see that the spacecraft jumps between resonant orbits using flybys at the moons. Although Ross and Lo's [2] trajectory was computed in the restricted five-body problem, Fig. 9b shows that the patched-CR3BP model is a good approximation and that the T-P graph captures the main dynamics; in fact, the spacecraft first shadows the T_M level sets of Callisto, then of Ganymede, and finally of Europa. The T-P graph also shows that the trajectory is quasi-ballistic. Another ballistic transfer is explained with the T-P graph in the Saturn–Titan system in [17].

Ballistic Endgame Paradox

Endgame or transfer trajectories designed with the linked-conics model always require some impulsive maneuver (Δv). The Δv is needed to increase/decrease the v_∞ from the escape/capture condition, because in general, the departure/arrival low-energy (low-V_∞) level sets do not intersect, as shown in Fig. 5a. To decrease the required Δv, a VILM strategy can be implemented using a sequence of almost resonant orbits and small maneuvers (i.e., a zigzag path in the r_a–r_p leveraging graph). For very long transfer times, a theoretical minimum Δv can be computed [1].

In the patched-CR3BP model, the T-P graph shows that the same low-energy (high Tisserand) level sets do indeed intersect. There might be endgames and transfers between moons that require little or no Δv and that consist of resonant orbits only; in fact, the multimoon orbiter trajectory [2] is one example of such a transfer.

An interesting paradox arises when considering *planar* ballistic endgames:

Paradox: Given a fixed Tisserand energy and arrival circular orbit altitude, the insertion maneuver costs remain essentially fixed for all possible arrival geometries.

The paradox seems to questions the utility of resonant orbits and of quasi-ballistic endgames in general. In what follows, we first prove the paradox and then we explain why resonant orbits are still necessary for the design of low-energy endgames.

Assume a ballistic endgame begins at Europa with a very high apocenter (for example, in the region II^e) and ultimately targets a low-altitude circular orbit (e.g., 100 km) at Europa. In the planar case, the orbit-insertion location is somewhere on a circle of radius $R_2 = r_\pi$ around Europa. Figure 10 shows the possible orbit-insertion locations as functions of the angle θ. In particular, in Fig. 10a the arrival conditions are represented in the rotating reference frame; in Fig. 10b the arrival conditions and the orbit-insertion maneuvers Δv_π are represented in the inertial moon-centered reference frame.

We now compute the orbit-insertion maneuver as a function of the angle θ for a given Jacobi constant and altitude at the moon. From simple geometric considerations,

$$R_1 = \sqrt{1 + r_\pi^2 + 2r_\pi \cos\theta} \tag{15}$$

$$R^2 = (1-\mu)^2 + r_\pi^2 + 2(1-\mu) r_\pi \cos\theta \tag{16}$$

Substituting Eqs. (15) and (16) in Eq. (4), we find that the velocity in the rotating frame is

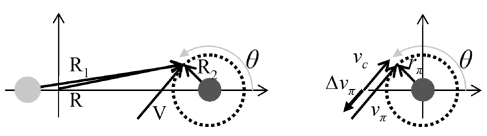

a) b)

Fig. 10 Possible orbit-insertion locations at the end of an endgame strategy.

$$V^2 = (1-\mu) + r_\pi^2 + 2(1-\mu) r_\pi \cos\theta + 2\frac{1-\mu}{\sqrt{1 + r_\pi^2 + 2 r_\pi \cos\theta}} + 2\frac{\mu}{r_\pi} - J \tag{17}$$

The velocity in the inertial frame is (see Appendix A)

$$v_\pi = (V + \sigma r_\pi) \tag{18}$$

The orbit insertion/escape Δv is

$$\Delta v_\pi = v_\pi - v_c = V + \sigma r_\pi - v_c \tag{19}$$

where $v_c = \sqrt{\mu / r_\pi}$. Then the orbit-insertion cost depends on V. It is easy to prove that $V^2(\theta)$ has a global maximum at $\theta = 0$ and a global minimum at $\theta = \theta^* = \arccos(-r_\pi/2)$. Also,

$$(V^2)_{\max} - (V^2)_{\min} = r_\pi^2 (1-\mu)\frac{3 + r_\pi}{1 + r_\pi}$$

and because r_π^2 is small compared with other terms in Eq. (17), we infer that $V_{\max} \approx V_{\min}$, i.e., the velocity and thus the orbit-insertion maneuver do not depend significantly on the angle θ. It would be interesting to know if the paradox extends to the 3-D case, in which

$$R^2 = 1 + r_\pi^2 \cos^2\alpha + 2 r_\pi \cos\theta \cos\alpha$$

$$R_1 = \sqrt{1 + r_\pi^2 + 2 r_\pi \cos\theta \cos\alpha}$$

and α is the elevation angle on the x–y plane. The velocity in the inertial frame has two components, i.e., V and $\omega \times r$, which are not aligned in general.

Table 1 shows $(\Delta v_\pi)_{\max}$ and $(\Delta v_\pi)_{\min}$ computed for $\theta = 0$ and $\theta = \theta^*$, respectively, for several cases of interest. We see that in all cases the difference in the orbit-insertion maneuver is just a few meters per second or less; thus, given a fixed energy, a ballistic endgame (which can only change θ) cannot reduce the cost significantly. A nonballistic endgame can reduce the orbit-insertion maneuver by applying impulsive Δv, which results in the highest change in the Jacobi constant. The VILM strategy can also be justified with this argument [18].

The paradox seems to question the utility of the ballistic endgame, at least in the planar case, because no matter how we design a sequence of resonant orbits, the orbit insertion Δv is fixed by the Jacobi constant and cannot change. We then wonder why we need resonant transfers in the first place.

The T-P graph clarifies this point and enables strategies for the design of low-cost quasi-ballistic endgames and transfers. A low-cost quasi-ballistic endgame at Europa, for example, must end with a low-Δv orbit insertion. Referring to Fig. 4, the corresponding T level sets will probably lie within region II^e. Because the endgame is quasi-ballistic, the initial conditions also lie in the region II^e, and according to the boundaries of the region II^e in Fig. 5, an initial high apocenter requires an initial high pericenter, beyond Europa's orbit. How can the spacecraft, then, ever reach a 100 km altitude to Europa, an impossible scenario based on the conventional wisdom of linked conics? The T-P graph shows, however, that if the spacecraft has the right phasing, it can use Europa perturbing force to slightly lower its apocenter *and* pericenter, thus moving to the left in the T-P graph, along the level set.

Table 1 Maximum and minimum orbit-insertion maneuvers (m/s) for given altitudes and Jacobi constant at Europa and at Titan

	$\Delta v_{\max}/\Delta v_{\min}$, km/s			
Moon	J_{L1}, 100 km	J_{L4}, 100 km	J_{L1}, 1000 km	J_{L4}, 1000 km
Europa	421.1/420.1	606.5/605.5	276.7/273.7	513.7/511.1
Titan	668.6/668.5	766.5/776.4	553.7/553.5	667.6/667.5

Such a maneuver is, in fact, a high-altitude flyby performed close to the pericenter of the spacecraft orbit. When several high-altitude flybys are linked together by free-return orbits, the pericenter can be lowered to the point at which a 100 km approach at Europa is possible. Thus, the high-altitude flybys are necessary *to reduce the pericenter* and to reach the required altitude at Europa, whereas the resonant orbits simply provide a mechanism to achieve multiple flybys. We note that energy levels of the endgame scenario require nonintersecting spacecraft and minor-body orbits (in the exterior problem, the spacecraft orbit engulfs completely the orbit of the minor body for all time, whereas the interior problem is reversed). Therefore, the point of closest approach for the two orbits occurs only at a single point in the nonrotating frame: the apse of the spacecraft orbit. Accordingly, the low-cost endgame return orbit must be approximately resonant, whereas a nonresonant returns would necessarily have two intersection points between the spacecraft and minor-body orbits.

An alternative way to explain the ballistic endgame is the following: of all the trajectories arriving at 100-km-alt at Europa with a fixed velocity defined by Eq. (18), the only one that starts at a very high apocenter must have performed several high-altitude flybys and resonant orbits. In the next section we use this concept to design ballistic transfers.

Design of Multibody Transfers with the T-P Graph

The previous section showed that even for low energy levels (i.e., Tisserand parameter between J_{L1} and 3) there can be trajectories that reach a low altitude at a moon, starting at a very high apocenter, through a sequence of flybys and resonant orbits. In this section we implement a simple search to find such trajectories and design low-cost transfers between Ganymede and Europa. A similar search was implemented in the design of the BepiColombo capture trajectory at Mercury [19]; in fact, at these energy levels, many ballistic capture or escape trajectories can be designed [20–22].

We first design a transfer between a 100-km-alt orbit at Ganymede and a 100-km-alt orbit at Europa. With this set of boundary conditions, we can compare the Δv of a Hohmann transfer to the Δv of the begin-game and endgame trajectories, designed using either the multibody technique or the VILM technique. However, we recall that longer times of flight yield to higher exposures to the radiation environment at Jupiter, so, in practice, longer-time-of-flight transfers are penalized by need of heavier shielding.

A direct Hohmann transfer from a 100-km-alt orbit at Ganymede to a 100-km-alt orbit at Europa requires only a few days, but costs 2.18 km/s. A VILM strategy can reduce this Δv up to a theoretical minimum of 1.71 km/s [1]. Using the T-P graph and the higher-fidelity CR3BP, we demonstrate how a low-cost transfer can require significantly less propellant.

The basic scheme for the design is shown in Fig. 11. We start by fixing an energy value for the escape and for the capture such that the spacecraft starts in the escape region II^e and ends in the capture region II^i. In particular, we choose

$$T \approx J = (J_{L2} + J_{L3})/2 \tag{20}$$

From the Jacobi constants, we find the velocities at pericenter using Eq. (18) [¶] and calculate the cost to insert into/escape from a circular orbit at 100 km altitude from Eq. (19): $\Delta v_{\text{escape}} \cong 0.72$ km/s and $\Delta v_{\text{capture}} \cong 0.51$ km/s. Immediately, we see that the floor for a potentially ballistic transfer Δv is $\Delta v_{\text{escape}} + \Delta v_{\text{capture}}$. We then scan the angles θ_{Ga}, propagate the initial conditions, and store the transfers that decrease the pericenter the most in the shortest time. We also scan the angles θ_{Eu}, *backward* propagate the initial conditions, and store the transfers that increase the apocenter the most in the shortest time. In both the forward and backward propagations, we have a precalculated target value for r_a and r_p, respectively (from the intersection point in the TP graph), found from the solution to Eq. (13).

[¶] In this example, we do not consider the retrograde solution.

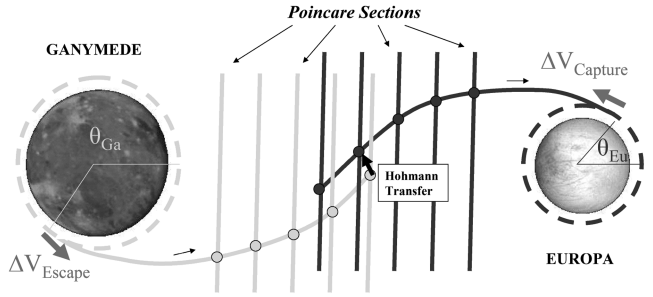

Fig. 11 Schematic of a transfer between Europa and Ganymede designed using the T-P graph.

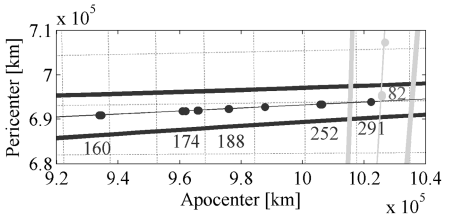

Fig. 12 Zoom of the T-P graph showing the Ganymede escape options and the Europa capture options.

We plot the results in the T-P graph. A close-up is shown in Fig. 12. In the graph we plot the level sets corresponding to the value of the Tisserand parameter in Eq. (20). One of the most important features of the T-P graph is the availability of a target pericenter–apocenter for both endgame and begin-game strategies, which is at the intersection of the level sets. For clarity, we do not plot all the Poincaré crossings from all the trajectories: we only plot the set of Pareto-optimal points (shortest time and highest apocenter) reached by all the solutions. Note that the final points of the begin-game and the initial points of the endgame do not coincide in general. Thus, some impulsive maneuvers are needed to patch the two parts of the transfer; the grid in the T-P graph provides a means to estimate a brute-force patching cost of a Hohmann-like transfer to connect the points in the graph. For instance, we can estimate a Δv of approximately 70 m/s to patch the 82-day begin-game with a 252-day endgame.

Among all the possible solutions on the graph, we choose the one with lower Δv, which takes $291 + 82$ days to transfer from Ganymede to Europa. In this case the T-P graph shows that very little Δv (approximately10 m/s) is required to patch the begin-game with the endgame. Then the total cost (TOT) of the transfer (to and from 100 km circular orbits) is mostly given by the escape and capture maneuver for a $\Delta v_{\mathrm{TOT}} \approx 1.25$ km/s: almost 500 m/s less than the VILM theoretical minimum Δv and almost 1 km/s less (but one year more) than the direct Hohmann transfer.

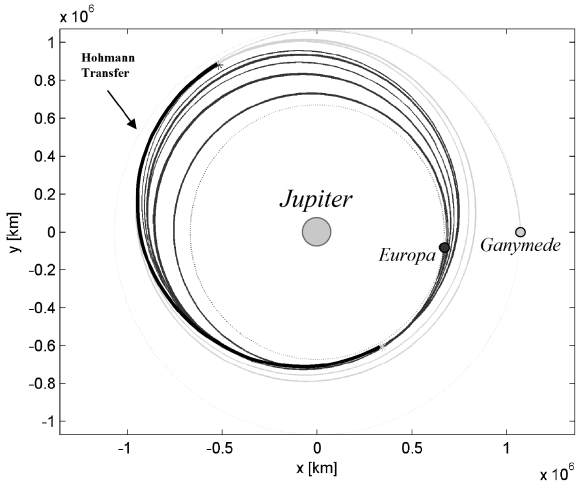

Fig. 13 Quasi-ballistic transfer in the inertial reference frame.

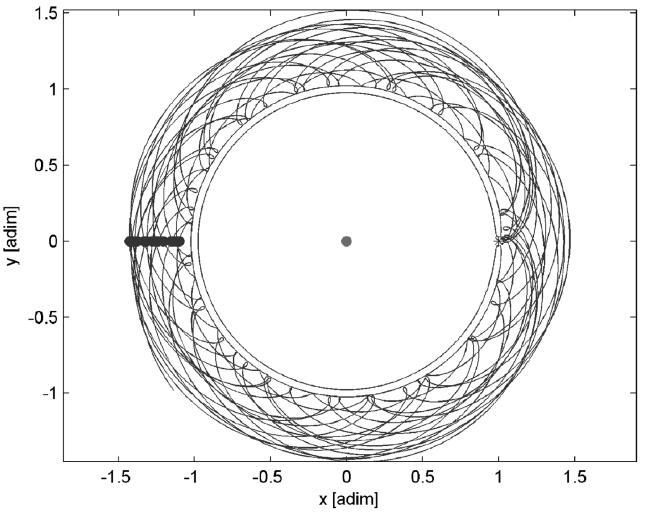

Fig. 14 Quasi-ballistic transfer in the rotating reference frame: the endgame at Europa.

Figure 13 shows the trajectory in the inertial reference frame centered at Jupiter. The figure also shows the Hohmann transfer, which patches the two parts of the trajectory. Figure 14 shows the endgame and Fig. 15 shows the begin-game part of this trajectory in the corresponding rotating reference frames. Figure 13 shows the same trajectories in the inertial reference frame centered at Jupiter. The figure also shows the Hohmann transfer that patches the two parts of the trajectory.

A typical mission to the moons of Jupiter would not include a 100 km science orbit at Ganymede, mainly because of the very high costs of the capture and escape Δv at Ganymede. For this reason, a more interesting case for a real mission is the transfer between a halo orbit around Europa and a halo orbit around Ganymede (although the time of flight must be limited because of the radiation exposure). In this case, the orbit insertion Δv and the orbit escape Δv are negligible, and the long transfer time is justified by a fully-quasi-ballistic transfer. The trajectories are computed in the patched spatial CR3BP, and the inclination at the Poincaré section never exceeds 1.5 deg.

To find suitable transfers, we scan the initial position along the initial and final halo orbits and perturb the starting conditions along the unstable and stable eigendirections, respectively. The initial halo orbit has a Jacobi constant in the Jupiter–Ganymede CR3BP of $J = 3.0052$, and the final halo orbit has a Jacobi constant in the Jupiter–Europa CR3BP of $J = 3.0023$. The energy levels are selected to be appropriate for ballistic transfers to high-altitude closed orbits about each moon [23].

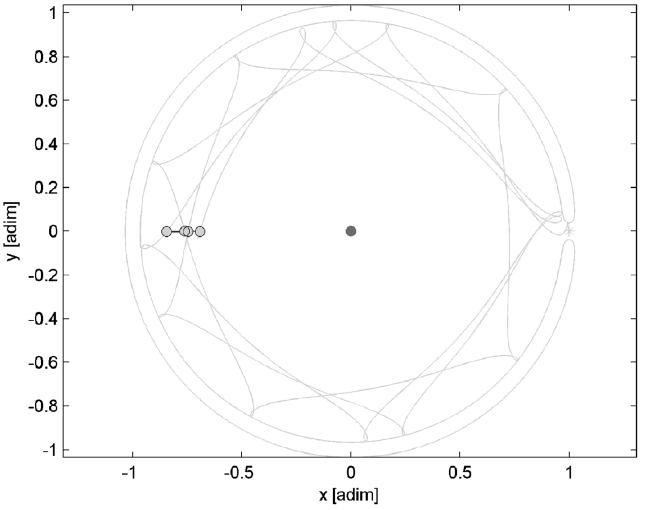

Fig. 15 Quasi-ballistic transfer in the rotating reference frame: the begin-game at Ganymede.

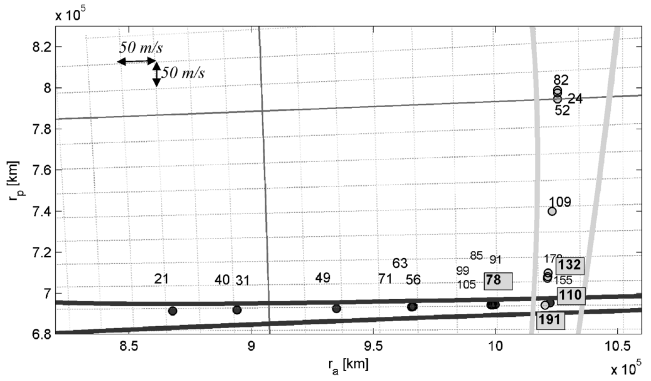

Fig. 16 T-P graph of the transfer from a halo orbit around Ganymede to a halo orbit around Europa; projection onto the $i = 0$ plane.

Of all the solutions found, we show one with a reasonably low flight time that comes close to hitting the target r_a–r_p intersection of (694,641 km, 1,021,834 km), found from the solution to Eq. (13). Figure 16 shows the T-P graph at $i = 0$ of the begin-game and of the endgame. For simplicity, the osculating pericenter and apocenter and inclination at the Poincaré section are projected on the $i = 0$ plane (we recall that the inclination never exceeds 1.5 deg) . The Ganymede begin-game takes 191 days to reach a very low pericenter, where it can be patched to the Europa endgame with a very little ΔV. The endgame lasts 110 days. Then the whole transfer takes less than 300 days (some initial revolutions are spent on the initial and final halos), and from the T-P graph we see that almost no ΔV is required to patch the two trajectories. Note that the begin-game could be reduced by two months with approximately an additional 50 m/s, resulting in a eight-month transfer from Ganymede to Europa. The begin-game can also be reduced by one month with an additional 50 m/s, resulting in a seven-month transfer that costs almost 100 m/s.

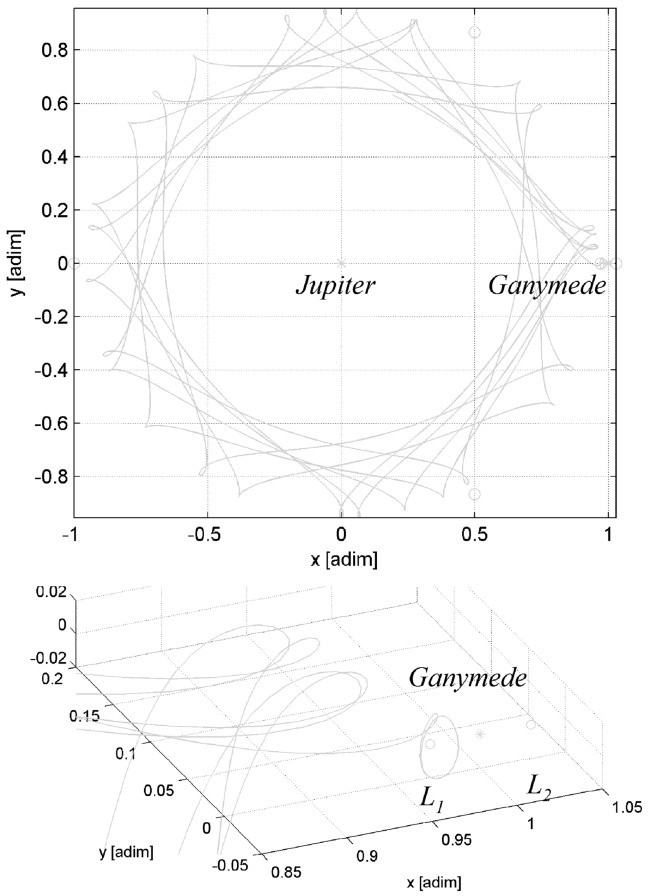

Fig. 17 Begin-game at Ganymede, the first part of the Ganymede to Europa transfer, in the rotating reference frame.

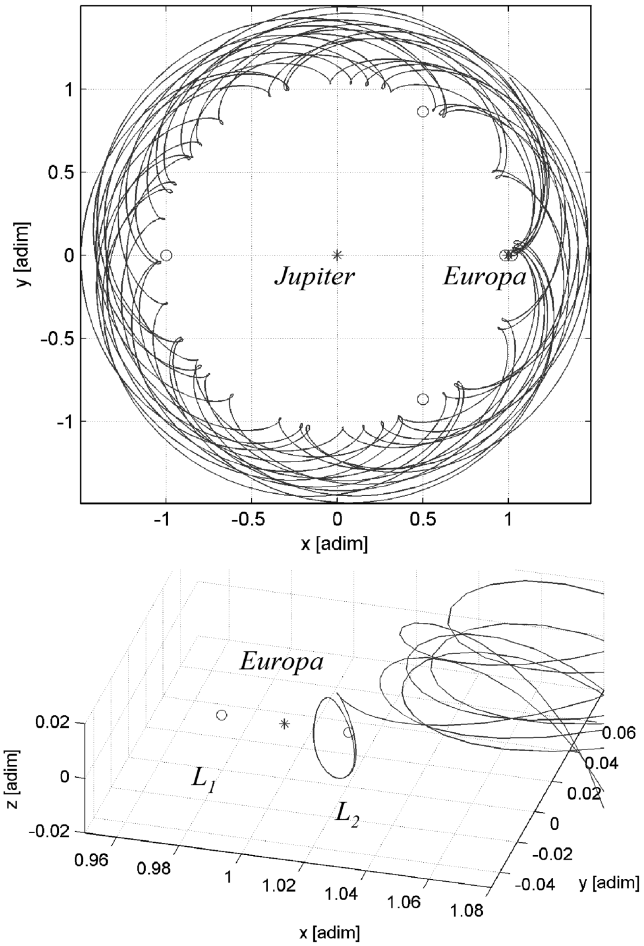

Fig. 18 Endgame at Europa, the second part of the Ganymede to Europa transfer, in the rotating reference frame.

The next figures show some details of the 300-day transfer. Figure 17 shows the begin-game in the Jupiter–Ganymede CR3BP, with a close-up of the escape from the halo orbit. Figure 18 shows the endgame in the Jupiter–Europa CR3BP, with a close-up of the capture into the halo orbit. In total, there are three high-altitude flybys of Ganymede and six high-altitude flybys of Europa.

In future works we plan to optimize this trajectory or similar ones in the full-ephemeris model. We do not expect the transfer time of the full-ephemeris trajectory to differ too much from the estimated value on the T-P graph. The total Δv might vary due to two important factors. On one hand, the Δv can increase due to change-of-plane maneuvers and fourth-body perturbations. On the other hand, we can reduce the Δv by inserting several midcourse maneuvers along the trajectory and using an optimizer to minimize the total cost. We can also reduce the Δv by fine-tuning the initial and final energies. Future works could also include explicit VILM-type maneuvers to shorten the time of flight of low-energy transfers.

We emphasize that the design approach outlined in this study requires no a priori knowledge of the resonant path and relies only on the chaotic nature of the CR3BP and fine-scale perturbations of the initial conditions. Future work includes methods that allow specification of the resonant paths to reduce the computation requirements and provide more systematic searches. Recent works in the field also suggest some ways to achieve this goal [24].

Conclusions

In this paper we present a new graphic tool, the Tisserand–Poincaré (T-P) graph, to understand and design low-cost endgames and transfers in the context of both linked-conics and patched-three-body systems. Although the T-P graph can be used like the Tisserand graph, it extends beyond the limits of the linked-conics approach into

the domain of the patched circular restricted three-body problem (CR3BP), showing that low-energy ballistic orbits around the moons are energetically connected. The T-P graph also provides target points and a simple rationale for the design of such transfers.

With a very simple search, we designed a transfer between a circular orbit at Europa and a circular orbit at Ganymede that requires only 1.25 km/s, almost 500 m/s less than the theoretical minimum cost achieved by v_∞-leveraging maneuver (VILM) transfers and almost 1 km/s less than the direct Hohmann transfer. With the same approach, we found a transfer between a halo orbit around L1 of the Ganymede–Jupiter system and a halo orbit around L2 of the Europa–Jupiter system. The transfer is quasi-ballistic and lasts 300 days and can be shortened by two months for an additional 50 m/s or shortened by three months for an additional 100 m/s.

In the future we plan to optimize these trajectories in the ephemeris model. The total Δv could decrease because of the optimization or increase due the effects that were neglected in the patched CR3BP. Many more solutions can be found using simple search approaches; however, we also envision using other more systematic techniques that use the T-P graph to design and patch resonant orbits, high-altitude flybys, and small midcourse maneuvers. Ideally, we would like to shorten the transfer times using VILM-type maneuvers in the patched CR3BP.

Appendix A: Coordinate Transformations

In this Appendix we recall the coordinate transformations for the CR3BP and some useful expressions used in the paper. The steps are standard and can be found in the literature [25].

We start by recalling the coordinate transformation from the rotating reference frame centered in the barycenter to the inertial reference frame centered in either body. We define the state vector in the rotating frame,

$$S = (X, Y, Z, \dot{X}, \dot{Y}, \dot{Z})^T \tag{A1}$$

the state vector in the inertial reference frame, centered in the barycenter,

$$s_{(B)} = (x_{(B)}, y_{(B)}, z_{(B)}, \dot{x}_{(B)}, \dot{y}_{(B)}, \dot{z}_{(B)})^T \tag{A2}$$

and the state vector in the inertial reference frame, centered in either body:

$$s = (x, y, z, \dot{x}, \dot{y}, \dot{z})^T \tag{A3}$$

We recall that all the variables are normalized using the scale factors defined in the paper, so that the angular velocity of the rotating frame is 1. Assuming that the rotating frame has no initial phase with respect to the inertial frame, the transformation from S to $s_{(B)}$ is given by

$$s_{(B)} = (X, Y, Z, \dot{X} - Y, \dot{Y} + X, \dot{Z})^T \tag{A4}$$

The transformation from $s_{(B)}$ to s is given by

$$s = (x_{(B)} - d, y_{(B)}, z_{(B)}, \dot{x}_{(B)}, \dot{y}_{(B)} - d, \dot{z})^T \tag{A5}$$

where $d = -\mu$ if the inertial reference frame is centered in the major body, and $d = 1 - \mu$ if the inertial reference frame is centered in the minor body.

Thus, the transformation from the rotating reference frame to the body-centered inertial reference frame and vice versa is given by the following equations:

$$(x, y, z, \dot{x}, \dot{y}, \dot{z})^T = (X - d, Y, Z, \dot{X} - Y, \dot{Y} + (X - d), \dot{Z})^T \tag{A6}$$

$$(X, Y, Z, \dot{X}, \dot{Y}, \dot{Z})^T = (x + d, y, z, \dot{x} + y, \dot{y} - x, \dot{z})^T \tag{A7}$$

In our work we are interested in the velocities in both reference frames. We first recall that the components of the velocity in the major/minor-body reference frame are related to the magnitude of the angular momentum and inclination of the spacecraft with respect to the major/minor body through

$$\dot{y}x - \dot{x}y = h \cos i \tag{A8}$$

We use Eqs. (A7) and (A8) to derive the an expression for the square of the velocity V^2:

$$\begin{aligned} V^2 &= \dot{X} + \dot{Y} + \dot{Z} = (\dot{x} + y)^2 + (\dot{y} - x)^2 + \dot{z}^2 \\ &= v^2 + (x^2 + y^2) - 2h \cos i \end{aligned} \tag{A9}$$

Now we consider the special case in which

$$s = (r_\pi \cos\theta, r_\pi \sin\theta, 0, -\sigma v_\pi \sin\theta, \sigma v_\pi \cos\theta, 0) \tag{A10}$$

where $\sigma = +1$ for direct orbits and $\sigma = -1$ for retrograde orbits, and $r_\pi = R_2$ is the distance from the minor body.

Applying Eq. (A7),

$$\begin{aligned} S = ((1 - \mu) + r_\pi \cos\theta, r_\pi \sin\theta, 0, -(\sigma v_\pi - r_\pi) \sin\theta, \\ (\sigma v_\pi - r_\pi) \cos\theta, 0) \end{aligned} \tag{A11}$$

so that

$$V = |\sigma v_\pi - r_\pi| = |v_\pi - \sigma r_\pi| \tag{A12}$$

Assuming $v_\pi > r_\pi$, we find

$$V = v_\pi - \sigma r_\pi, \qquad v_\pi = V + \sigma r_\pi \tag{A13}$$

Appendix B: Tisserand Parameter, Jacobi Constant, and V_∞

For completeness, in this Appendix we derive the Tisserand parameter from the Jacobi constant. Similar derivations can be found in the literature [11,12].

Using Eqs. (A7) and (A9) we express the Jacobi constant in the inertial reference frame centered in the major body:

$$\begin{aligned} J = ((x - \mu)^2 + y^2) + 2\frac{1 - \mu}{r} + 2\frac{\mu}{R_2} \\ + (1 - \mu)\mu - V^2 - r^2 + 2h \cos i \end{aligned} \tag{A14}$$

Using the vis-viva equation and the expression for the angular momentum

$$V^2 = 2\frac{1 - \mu}{r} - \frac{1 - \mu}{a} \tag{A15}$$

$$h = \sqrt{a(1 - e^2)(1 - \mu)} \tag{A16}$$

we find

$$\begin{aligned} J = \frac{1 - \mu}{a} + 2\sqrt{a(1 - e^2)(1 - \mu)} \cos i + 2\frac{\mu}{R_2} - x\mu \\ + \mu^2 + (1 - \mu)\mu \end{aligned} \tag{A17}$$

If we let $\mu \to 0$, and assuming R_2 is not too small (as in the case when far from the minor body), Eq. (A17) becomes

$$J \approx \frac{1}{a} + 2\sqrt{a(1 - e^2)} \cos i = T \tag{A18}$$

Now we assume that the spacecraft's orbit crosses the minor-body orbit. At the crossing point, we can write the v_∞ as

$$v_\infty^2 = 1 + v^2 - 2v \cos\gamma \cos i \tag{A19}$$

where γ is the flight-path angle. We recall the vis-viva equation for $r = 1$ and $\mu \to 0$ and the expression of the angular momentum

$$\frac{1}{a} = 2 - v^2, \qquad h = v\cos\gamma \tag{A20}$$

to find

$$\frac{1}{a} = 2 - v_\infty^2 + 1 - 2h\cos i \tag{A21}$$

substituting Eq. (A21) into Eq. (A18), we finally find

$$J \approx T = 3 - v_\infty^2 \tag{A22}$$

Acknowledgments

The authors would like to thank Jon Sims [Jet Propulsion Laboratory, California Institute of Technology (JPL)], Nathan Strange (JPL), Anastassios Petropoulos (JPL), Arnaud Boutonnet (ESA), Shane Ross (Virginia Polytechnic Institute and State University), Martin Gehler (RWTH Aachen University), and Evan Gawlik (California Institute of Technology) for their valuable comments.

References

[1] Campagnola, S., and Russell, R. P., "Endgame Problem Part 1: V-Infinity Leveraging Technique and the Leveraging Graph," *Journal of Guidance, Control, and Dynamics*, Vol. 33, No. 2, March–April 2009, pp. 463–475. doi:10.2514/1.44258

[2] Ross, S. D., and Lo, M. W., "Design of a Multi-Moon Orbiter," *Advances in the Astronautical Sciences*, Vol. 114, Univelt, San Diego, CA, 2003, pp. 669–684; also American Astronautical Society Paper 03-143.

[3] Boutonnet, A., de Pascale, P., and Canalias, E., "Design of the Laplace Mission," 59th International Astronautical Congress, International Astronautical Federation, Paper 08-C1.6, Glasgow, Scotland, U.K., 2008.

[4] Johannesen, J. R., and D'Amario, L. A., "Europa Orbiter Mission Trajectory Design," *Advances in the Astronautical Sciences*, Vol. 103, Pt. 3, Univelt, San Diego, CA, 1999, pp. 895–908; also American Astronautical Society Paper 99-360.

[5] Schoenmaekers, J., Pulido, J., and Cano, J., "SMART-1 Moon Mission: Trajectory Design Using the Moon Gravity," ESA TR SI-ESC-RP-5501, European Space Operation Center, Darmstadt, Germany, 1999.

[6] Szebehely, V., *Theory of Orbits. The Restricted Problem of Three Bodies*, Academic Press, New York, 1967, pp. 557–587.

[7] Jacobi, C. G. J., "Sur le Movement d'un Point et sur un cas Particulier du Probleme des Trois Corps," *Comptes Rendus de l'Académie des Sciences de Paris*, Vol. 3, 1836, pp. 59–61.

[8] Ross, S. D., and Scheeres, D. J, "Multiple Gravity Assists, Capture, and Escape in the Restricted Three-Body Problem," *SIAM Journal on Applied Dynamical Systems*, Vol. 6, No. 3, Jan. 2007, pp. 576–596. doi:10.1137/060663374

[9] Labunsky, A., Papkov, O., and Sukhanov, K., *Multiple Gravity Assist Interplanetary Trajectories*, Earth Space Institute Book Series, Gordon and Breach, London, 1998, pp. 33–68.

[10] Strange, N. J., and Longuski, J. M., "Graphical Method for Gravity-Assist Trajectory Design," *Journal of Spacecraft and Rockets*, Vol. 39, No. 1, 2002, pp. 9–16. doi:10.2514/2.3800

[11] Tisserand, F. F., *Traité de Méchanique Céleste*, Vol. 4, Gauthier-Villars, Paris, 1896, pp. 203–205.

[12] Miller, J. K., and Weeks, C. J., "Application of Tisserand's Criterion to the Design of Gravity Assist Trajectories," AAS/AIAA Astrodynamics Specialist Conference and Exhibit, AIAA Paper 2002-4717, Aug. 2002.

[13] Ross, S. D., Jerg, S., and Junge, O., "Optimal Capture Trajectories Using Multiple Gravity Assists," *Communications in Nonlinear Science and Numerical Simulation*, Vol. 14, No. 12, 2009, pp. 4168–4175. doi:10.1016/j.cnsns.2008.12.009

[14] Gehler, M., "On Transport and Collision of near-Earth Objects Using Restricted Dynamical Systems," M.S., Thesis, Inst. of Aeronautics and Astronautics, RWTH Aachen Univ., Aachen, Germany, 2009.

[15] Janin, G., Boutonnet, A., and Campagnola, S., "Solar Orbiter Mission Analysis," ESA TR WP 481, European Operation Center, Darmstadt, Germany, March 2005.

[16] Murray, C. D., and Dermott, S. F., *Solar System Dynamics*, Cambridge Univ. Press, New York, Feb. 2000, pp. 456–467.

[17] Gawlik, E. S., Marsden, J. E., Campagnola, S., and Moore, A., "Invariant Manifolds, Discrete Mechanics, and Trajectory Design for a Mission to Titan," AAS/AIAA Space Flight Mechanics Meeting, American Astronautical Society Paper 09-226, Savannah, GA, Feb. 2009.

[18] Sweetser, T. H., "Jacobi's Intergal and DV-Earth- Gravity Assist (DV-EGA) Trajectories," *Advances in the Astronautical Sciences*, Vol. 85, Univelt, San Diego, CA, 1993, pp. 417–430; also American Astronautical Society Paper 93-635.

[19] Jehn, R., Campagnola, S., Garcia, D., and Kemble, S., "Low-Thrust Approach and Gravitational Capture at Mercury," *ESA Special Publication for the 18th International Symposium on Space Flight Dynamics*, Vol. 548, ESA Publications Div., Noordwijk, The Netherlands, 2004, p. 487.

[20] Campagnola, S., and Lo, M. W., "BepiColombo Gravitational Capture and the Elliptic Restricted Three-Body Problem," *Proceedings in Applied Mathematics and Mechanics*, Vol. 7, No. 1, 2008, pp. 1030905–1030906, Aug. 2008. doi:10.1002/pamm.200700330

[21] Paskowitz, M. E., and Scheeres, D. J., "Robust Capture and Transfer Trajectories for Planetary Satellite Orbiters," *Journal of Guidance, Control, and Dynamics*, Vol. 29, No. 2, 2006, pp. 342–353. doi:10.2514/1.13761

[22] Villac, B. F., and Scheeres, D. J., "Escaping Trajectories in the Hill Three Body Problem and Application," *Journal of Guidance, Control, and Dynamics*, Vol. 26, No. 2, 2003, pp. 224–232. doi:10.2514/2.5062

[23] Russell, R. P., and Lam, T., "Designing Ephemeris Capture Trajectories at Europa Using Unstable Periodic Orbits," *Journal of Guidance, Control, and Dynamics*, Vol. 30, No. 2, 2007, pp. 482–491. doi:10.2514/1.22985

[24] Grover, P., and Ross, S. D., "Designing Trajectories in a Planet-Moon Environment Using the Controlled Keplerian Map," *Journal of Guidance, Control, and Dynamics*, Vol. 32, No. 2, 2009, pp. 437–444. doi:10.2514/1.38320

[25] Anderson, R. L., "Low Thrust Trajectory Design for Resonant Flybys and Captures Using Invariant Manifolds," Ph.D. Thesis, Univ. of Colorado at Boulder, Boulder, CO, 2005.